LA-UR-15-27896
Approved for public release; distribution is unlimited.

Title: A defect density-based constitutive crystal plasticity framework for modeling the plastic deformation of Fe-Cr-Al cladding alloys subsequent to irradiation

Author(s): Patra, Anirban
Wen, Wei
Martinez Saez, Enrique
Tome, Carlos

Intended for: Report

Issued: 2016-02-05 (rev.1)

A defect density-based constitutive crystal plasticity framework for modeling the plastic deformation of Fe-Cr-Al cladding alloys subsequent to irradiation

Anirban Patra, Wei Wen, Enrique Martínez, Carlos Tomé

Materials Science and Technology Division, Los Alamos National Laboratory

Los Alamos, NM 87545

Report on Milestone:

M3MS-15LA0201069: Calculation of irradiation hardening laws

LANL-ATF Assessments (MS-15LA020106)

September 24, 2015

A defect density-based constitutive crystal plasticity framework for modeling the plastic deformation of Fe-Cr-Al cladding alloys subsequent to irradiation

Anirban Patra, Wei Wen, Enrique Martínez, Carlos Tomé

Materials Science and Technology Division, Los Alamos National Laboratory

Los Alamos, NM 87545

1. Introduction

Cladding materials used in nuclear reactors undergo significant radiation damage over the course of their life. Radiation damage leads to the creation of complex defect microstructures comprising of defect clusters, interstitial loops, dislocation substructures, etc. [1]. This in turn influences the deformation behavior, manifested in terms of irradiation-induced hardening, significant loss of ductility [2], [3], and accelerated creep rates at relatively lower temperatures [4], [5]. This is a matter of concern for the reactor conditions of high temperature and oxidation environment under mechanical loading.

While previous generation reactors have primarily used Zr-alloys for the cladding [6], recent research has been directed towards exploring new candidates for cladding materials, which are more tolerant to accident conditions, Loss of Coolant Accident (LOCA) for example. Fe-Cr alloys have been extensively studied as potential cladding materials for fast reactors primarily because of their swelling resistance and increase in thermal conductivity [2], [7]. More recently, there has been interest in Fe-Cr-Al alloys as cladding materials for light water reactors, because the addition of Al provides enhanced oxidation resistance in steam at higher temperatures [8].

It is essential to understand the deformation behavior of these Fe-Cr-Al alloys, in order to be able to develop models for predicting their mechanical response under varied loading conditions. Interaction of dislocations with the radiation-induced defects governs the crystallographic deformation mechanisms. A crystal plasticity framework is employed to model these mechanisms in Fe-Cr-Al alloys. This work builds on a previously developed defect density-based crystal plasticity model for bcc metals and alloys [9], [10], with necessary modifications made to account for the defect substructure observed in Fe-Cr-Al alloys. The model is implemented in a Visco-Plastic Self Consistent (VPSC) framework [11], [12] to predict the mechanical behavior under quasi-static loading.

2. Model Description

Crystal Plasticity Kinematics

The VPSC formulation models deformation at the level of grains (single crystals) in terms of the plastic deformation gradient, $\boldsymbol{F}^{p}$, neglecting the effects of elastic deformation on the crystal. The time rate of deformation gradient is given as

$$\dot{\boldsymbol{F}}^{p} = \boldsymbol{L}^{p} \cdot \boldsymbol{F}^{p} \tag{1}$$

where, $\boldsymbol{L}^{p}$ is the plastic velocity gradient, given by the tensor sum of crystallographic shearing rates, $\dot{\gamma}^{\kappa}$, over all slip systems present in the crystal, i.e.,

$$\boldsymbol{L}^{p} = \sum_{\kappa} \dot{\gamma}^{\kappa} \boldsymbol{m}^{\kappa} \otimes \boldsymbol{n}^{\kappa} \tag{2}$$

Here, $\boldsymbol{m}^{\kappa}$ is unit vector corresponding to the slip direction, and $\boldsymbol{n}^{\kappa}$ is the unit vector corresponding to the slip plane normal. The crystallographic shearing rate is a function of the resolved shear stress, τ^{κ}, and the internal state variables in the model. Here we focus on instantaneous plasticity taking place in an irradiated material; dislocation climb associated with irradiation and thermal creep is not accounted for.

Internal State Variables

Primary irradiation-induced defect structures observed in Fe-Cr-Al alloys include: <111> dislocation loops, <100> dislocation loops, and α' precipitates [13], [14], in addition to the line dislocations present in the microstructure. Accordingly, the following internal state variables (ISVs) are used at the level of slip system, κ, in our crystal plasticity framework:

1. Mobile dislocation density, ρ_{M}^{κ},
2. Immobile dislocation density, ρ_{I}^{κ},
3. Number density, N_{111}^{κ}, and size, d_{111}^{κ}, of <111> dislocation loops,
4. Number density, N_{100}^{κ}, and size, d_{100}^{κ}, of <100> dislocation loops, and
5. Number density, $N_{\alpha'}^{\kappa}$, and size, $d_{\alpha'}^{\kappa}$, of α' precipitates.

Further, experimental microscopy has also found indistinguishable dislocation loops (with respect to the Burgers vector), commonly referred as black dots [14], in the post-irradiated microstructure. Following Ref. [14], it is assumed that the black dot population is equally distributed among the <111> and <100> dislocation loop densities. The evolution and interaction of these ISVs is assumed to govern plastic deformation.

Crystallographic Shearing Rate

Plastic deformation in metallic crystals is governed by the glide of dislocations on closed packed planes (slip planes). This is manifested in a crystal plasticity framework in terms of the crystallographic shearing rate, $\dot{\gamma}^{\kappa}$. While various constitutive model forms exist for $\dot{\gamma}^{\kappa}$, the commonly used power law model is used here to model shearing rate as a function of the resolved shear stress, such that:

$$\dot{\gamma}^{\kappa} = \dot{\gamma}_{0} \left(\frac{\left| \tau^{\kappa} \right|}{\tau_{0}^{\kappa}} \right)^{n} \operatorname{sgn}\left(\tau^{\kappa} \right) \tag{3}$$

where, $\dot{\gamma}_0$ is the reference shear rate, τ_0^κ is the slip resistance, and n is the inverse of strain rate sensitivity. Note that this flow rule is a special case of the Kocks-type activation energy driven model for slip (cf. [15]), which models the shearing rate as a statistical ensemble average of the dislocation glide events achieved by overcoming the temperature- and stress-dependent energy barrier. Future work will model the crystallographic shearing rate in this more comprehensive form to account for thermal effects on mitigating the energy barrier for dislocation glide. Also note that non-Schmid effects on constricting the dislocation core of the plasticity-governing screw dislocations in bcc metals [16]–[18] are neglected in the present formulation.

Lattice Resistance

The contributions to slip resistance, τ_0^κ, are assumed to be: the intrinsic frictional resistance, σ_0, the Hall-Petch term accounting for grain size dependence [19], [20], $\sigma_{HP} = k_{HP}/\sqrt{D}$ (k_{HP} is a material constant, D is the grain size), and the lattice resistance to dislocation glide due to long range interactions, σ_{LR}^κ, with other dislocations, dislocation loops, and α' precipitates. A dispersed barrier hardening model [21], [22] is used to model these long range interactions, such that:

$$\sigma_{LR}^\kappa = Gb\left(h_\rho \sqrt{\sum_\zeta A_{\kappa\zeta}\left(\rho_M^\zeta + \rho_I^\zeta\right)} + h_{111}\sqrt{N_{111}^\kappa d_{111}^\kappa} + h_{111}\sqrt{N_{100}^\kappa d_{100}^\kappa} + h_{\alpha'}\sqrt{N_{\alpha'}^\kappa d_{\alpha'}^\kappa} \right) \tag{4}$$

where, G is the shear modulus, b is the Burgers vector magnitude, $A_{\kappa\zeta}$ is the matrix of slip system dislocation interaction coefficients (to model self and latent hardening), and h_ρ, h_{111}, h_{100}, $h_{\alpha'}$ are the hardening coefficients associated with line dislocations, <111> dislocation loops, <100> dislocation loops, and α' precipitates, respectively.

Accordingly, the total slip resistance on slip system, κ, has the following form:

$$\tau_0^\kappa = \sigma_0 + \sigma_{HP} + \sigma_{LR}^\kappa \tag{5}$$

Substructure Evolution

This section will first describe the evolution of line dislocations, followed by the evolution of irradiation-induced dislocation loops and α' precipitates during plastic deformation.

Mobile dislocations are assumed to evolve primarily via three mechanisms [10]: creation of mobile dislocations via multiplication at existing dislocation segments, mutual annihilation of dislocation dipoles, and trapping of mobile dislocation segments at barriers, thus rendering them immobile. Dynamic recovery of immobile dislocations may lead to depletion of the immobile dislocation population. Accordingly, the net rate of evolution of mobile and immobile dislocations is given as

$$\dot{\rho}_M^\kappa = \frac{k_{mul}}{b l_d}\left|\dot{\gamma}^\kappa\right| - \frac{2R_c}{b}\rho_M^\kappa\left|\dot{\gamma}^\kappa\right| - \frac{1}{b\lambda^\kappa}\left|\dot{\gamma}^\kappa\right| \tag{6}$$

$$\dot{\rho}_I^{\kappa} = \frac{1}{b\lambda^{\kappa}}\left|\dot{\gamma}^{\kappa}\right| - k_{dyn}\rho_I^{\kappa}\left|\dot{\gamma}^{\kappa}\right| \tag{7}$$

where, k_{mul} is a material constant associated with dislocation multiplication, $l_d = 1/\sqrt{\sum_{\zeta}\rho_M^{\zeta} + \rho_I^{\zeta} + N_{111}^{\zeta}d_{111}^{\zeta} + N_{100}^{\zeta}d_{100}^{\zeta}}$ is the total line length of dislocations [23], R_c is the capture radius associated with mutual annihilation of mobile dislocations (the factor of 2 accounts for the fact that two dislocations are annihilated during this event) [24], λ^{κ} is the effective mean free path of trapping mobile dislocations at barriers, given by [25], [26]

$$\frac{1}{\lambda^{\kappa}} = \frac{1}{\lambda_{\rho}^{\kappa}} + \frac{1}{\lambda_{111}^{\kappa}} + \frac{1}{\lambda_{100}^{\kappa}} + \frac{1}{\lambda_{\alpha'}^{\kappa}} = \beta_{\rho}\sqrt{\rho_M^{\kappa} + \rho_I^{\kappa}} + \beta_{111}\sqrt{N_{111}^{\kappa}d_{111}^{\kappa}} + \beta_{100}\sqrt{N_{100}^{\kappa}d_{100}^{\kappa}} + \beta_{\alpha'}\sqrt{N_{\alpha'}^{\kappa}d_{\alpha'}^{\kappa}} \tag{8},$$

and k_{dyn} is the material constant associated with dynamic recovery. β_{ρ}, β_{111}, β_{100}, and $\beta_{\alpha'}$ are the trapping coefficients associated with line dislocations, <111> dislocation loops, <100> dislocation loops, and α' precipitates, respectively. Detailed description of the physical mechanisms behind these models is given in Ref. [10].

Interaction of mobile dislocations with the irradiation-induced defects is not completely understood presently and is a matter of ongoing research (via experimental microscopy [27]–[30] and lower scale simulations [31]–[35]). It is however known that mobile dislocations, with sufficient driving force, eventually annihilate/sweep away these defects [36], [37], leading to the formation of defect-free dislocation channels along favored crystallographic directions [38], [39] and subsequent flow localization along these channels [40], [41]. This is modeled using a previously developed phenomenological model [9] that accounts for the annihilation rate of irradiation-induced defects as a function of the crystallographic defect density and the interacting mobile dislocation density. Accordingly, the rate of annihilation of the areal density of irradiation-induced defects is given as [9]

$$\dot{N}_{111}^{\kappa}d_{111}^{\kappa} = -\frac{R_{111}^{\kappa}}{b}\left(N_{111}^{\kappa}d_{111}^{\kappa}\right)^{c}\left(\rho_M^{\kappa}\right)^{1-c}\left|\dot{\gamma}^{\kappa}\right| \tag{9}$$

$$\dot{N}_{100}^{\kappa}d_{100}^{\kappa} = -\frac{R_{100}^{\kappa}}{b}\left(N_{100}^{\kappa}d_{100}^{\kappa}\right)^{c}\left(\rho_M^{\kappa}\right)^{1-c}\left|\dot{\gamma}^{\kappa}\right| \tag{10}$$

$$\dot{N}_{\alpha'}^{\kappa}d_{\alpha'}^{\kappa} = -\frac{R_{\alpha'}^{\kappa}}{b}\left(N_{\alpha'}^{\kappa}d_{\alpha'}^{\kappa}\right)^{c}\left(\rho_M^{\kappa}\right)^{1-c}\left|\dot{\gamma}^{\kappa}\right| \tag{11}$$

where, c is the annihilation exponent, and R_{111}^{κ}, R_{100}^{κ}, and $R_{\alpha'}^{\kappa}$ are the capture radii associated with the annihilation of <111> loops, <100> loops, and α' precipitates, respectively. The capture radii associated with the various types of defects may be physically expected to be of the order of the corresponding defect sizes. Note that no distinction is made between the different

types of defects, with respect to their annihilation mechanism. At this moment, not enough experimental/atomistic insight is available to distinguish this. Further, the α' precipitates are assumed to be annihilated along with the <111> and <100> dislocation loops, based on the fact that the dislocation channels are typically cleared of all type of defects. A recent dislocation dynamics study has suggested that the interaction of loops (primarily <111> loops were studied) with mobile dislocations might lead to the loops 'transforming' to forest dislocations with lower hardening resistance and eventual flow localization [42]. However, at this moment it is not understood if a similar 'transformation' occurs for loops with <100> Burgers vector, as well. Studying the interaction between <100> loops and line dislocations is a subject of the current NEAMS Project.

3. Brief Description of the VPSC Framework

The visco-plastic self-consistent (VPSC) framework is used to relate the macroscopic polycrystal deformation to the individual grains deformation. The self-consistent model assumes that each grain can be considered as an inhomogeneous inclusion embedded in an effective medium having the average properties of all grains in the aggregate. A detailed description of the VPSC model can be found in Refs. [43], [44]. The plastic deformation in each grain occurs via the activation of slip and/or twin systems. The total strain rate on a given grain is given by the combined contribution of the shear rates of all slip and twinning systems, and the latter are related to the stress in the grain through the constitutive law:

$$\dot{\varepsilon}_{ij}^{g} = \sum_{s} m_{ij}^{s} \dot{\gamma}^{s} = \dot{\gamma}_0 \sum_{s} m_{ij}^{s} \left(\frac{m_{kl}^{s} : \sigma_{kl}^{g}}{\tau^{s}} \right)^{n} \tag{12}$$

where, $m_{ij}^{s} = \frac{1}{2}\left(n_i^{s} b_j^{s} + n_j^{s} b_i^{s} \right)$ is the symmetric Schmid tensor associated with slip system s; $\overline{n}^{s}$ and $\overline{b}^{s}$ are the normal and burgers vector of the system; $\dot{\varepsilon}_{ij}^{g}$ and σ_{kl}^{g} are the deviatoric strain-rate and stress of the grain, $\dot{\gamma}_0$ is the normalization rate and n is the rate sensitivity exponent. The linearized form for the constitutive law of the single crystal response is:

$$\dot{\varepsilon}_{ij}^{g} = M_{ijkl}^{g}\left(\sigma^{g} \right) \sigma_{kl}^{g} + \dot{\varepsilon}_{ij}^{0,g} \tag{13}$$

where, M_{ijkl}^{g} and $\dot{\varepsilon}_{ij}^{0,g}$ are the visco-plastic compliance and the back-extrapolated rate of grain g, respectively. Depending on the linearization assumption chosen, Eq. (13) gives a response that goes from the stiff secant to the compliant tangent approximation [43]. For an affine linearization (the kind used in the present work), the actual grain level compliance is used, i.e.,

$$M_{ijkl}^{g} = n\dot{\gamma}_0 \sum_{s} \frac{m_{ij}^{s} m_{kl}^{s}}{\tau_{s}^{0}} \left(\frac{m_{pq}^{s} \sigma_{pq}^{g}}{\tau_{s}^{0}} \right)^{n-1} \tag{14}$$

$$\dot{\varepsilon}_{ij}^{0,g} = \left(1-n\right)\dot{\varepsilon}^{g} \tag{15}$$

Performing homogenization on this linearized heterogeneous medium consists of assuming that a linear relation analogous to Eq. (13) is valid at the effective medium (polycrystal) level:

$$\bar{\dot{\varepsilon}}_{ij} = \bar{M}_{ijkl}(\bar{\sigma})\,\bar{\sigma}_{kl} + \bar{\dot{\varepsilon}}_{ij}^{0} \tag{16}$$

where, $\bar{\dot{\varepsilon}}_{ij}$ and $\bar{\sigma}_{kl}$ are the macroscopic rate and stress, and $\bar{M}_{ijkl}$ and $\bar{\dot{\varepsilon}}_{ij}^{0}$ are the macroscopic viscoplastic compliance and back extrapolated rate, respectively. Solving the stress equilibrium equation of an ellipsoidal inclusion described by Eq. (13) embedded in a medium described by Eq. (16) leads to the so called 'interaction equation' relating macroscopic and inclusion magnitudes

$$(\dot{\varepsilon}_{ij} - \bar{\dot{\varepsilon}}_{ij}) = -\tilde{M}_{ijkl}\,(\sigma_{kl} - \bar{\sigma}_{kl}) \tag{17}$$

where,

$$\tilde{M}_{ijkl} = \left(I - S\right)^{-1}_{ijmn} S_{mnpq}\,\bar{M}_{pqkl} \tag{18}$$

is the 'interaction tensor'. Depending on the linearization assumption chosen, $\bar{M}$ varies between the upper bound compliance $\bar{M}^{\text{tangent}}$ and the lower bound compliance, $\bar{M}^{\text{secant}} = \bar{M}^{\text{tangent}} \big/ n$.

The macroscopic moduli are unknown *a priori* and need to be adjusted self-consistently by enforcing the condition that the average stress and strain rate over all grains has to be equal to the macroscopic stress and strain rate:

$$\bar{\dot{\varepsilon}}_{ij} = \left\langle \dot{\varepsilon}_{ij} \right\rangle, \quad \sigma_{ij} = \left\langle \sigma_{ij} \right\rangle \tag{19}$$

The conditions in Eq. (19), along with grain strain rate and stress given by the visco-plastic inclusion formalism, define what is called a 'self-consistent visco-plastic' polycrystal model. Substituting Eqs. (13) and (16) in Eq. (19) leads to an expression for the visco-plastic moduli of the linearized effective medium [43].

4. Parameter Estimation

There is very limited experimental data in the literature regarding the deformation behavior of these (in development) Fe-Cr-Al alloys.

Recent experiments at Oak Ridge National Laboratory [45] have characterized the tensile response of laser weld specimens of virgin (without irradiation), cold worked Fe-Cr-Al alloys. The room temperature true stress-strain curves were generated using Digital Image Correlation (DIC) techniques for the parent material and the material at the fusion zone. Essentially the parent material has a higher density of stored dislocations and smaller grain size due to the prior cold work. The fusion zone material on the other hand has undergone dislocation recovery and

has a larger average grain size as a consequence of the 'heat treatment' during the welding process. These experimental true stress-strain curves [45] have been used to calibrate our model parameters for the virgin material.

In another set of experiments by the same group [13], [14], the tensile response of cold worked Fe-Cr-Al alloys with varying composition and irradiated to 1.6 dpa damage was reported. However, these experimental data are limited in usability since only the engineering stress-strain response was reported. As mentioned earlier, localized deformation commences at a much earlier stage (3-4% strain) in irradiated specimens, as compared to virgin specimens, due to the formation of dislocation channels. This prevents us from interpreting the true stress-strain response beyond the point of initiation of localized deformation. Moreover, the experimental data reported in Ref. [14] seems to have a much lower modulus in the elastic region than expected, suggesting that loading train deformation may be contributing. Nevertheless, experimental microscopy was used to characterize the densities of the irradiation-induced defects for the various alloy compositions in this work [13], [14]. These defect densities were used as input variables for our model and the resulting increase in yield stress was compared to the experiments at 1.6 dpa damage.

Model parameters relating to the physical constants such as shear modulus and Burgers vector magnitude were adopted from the corresponding values of pure bcc-iron. Using the defect densities from the aforementioned experimental studies, parameters relating to the initial yield stress were first calibrated to match experiments. In all cases, an initial mobile dislocation density of $1.0\times10^{11}\mathrm{m}^{-2}$ was assumed on all 24 {110}<111> and {112}<111> slip systems present in the bcc material. An equal distribution of immobile dislocation density was assumed on all slip systems using the experimentally reported line dislocation densities for the cold worked alloys in Ref. [14]. These are of the order of $10^{12}-10^{13}\mathrm{m}^{-2}$ per slip system. Note that the assumption of an equal dislocation density on all slip systems needs to be modified to account for the fact that a higher degree of slip is observed on {110} slip systems, as compared to {112} slip systems during plastic deformation (cf. [46]). We will address this in future work. The dislocation density of the fusion zone material was not reported in the experiments and it was assumed to be an order of magnitude lower than the corresponding cold worked material, to represent an effectively annealed material.

Using this information, model parameters relating to the evolution of mobile and immobile dislocation densities in Eqs. (6) and (7) were first calibrated. Following this, model parameters relating to irradiation hardening and defect evolution were calibrated. Note that the experiments report the mechanical response for just one radiation dose (1.6 dpa), where the α' precipitates were found to be the dominant radiation-induced defects [13], [14]. More experimental data, perhaps at higher radiation doses, is needed to quantify the substructure evolution parameters relating to irradiation-induced defects with a higher degree of confidence. Caveats notwithstanding, the parameters estimated from this initial calibration process are given in Table 1. Table 2 gives the defect densities for the various alloys, both virgin and irradiated, used in our model.

It should be noted that in this initial implementation, we have estimated our model parameters based solely on fit to experiments. In the next phase of the project, we will use dislocation dynamics simulations to study to the interaction of line dislocations with radiation-induced defects, such as dislocation loops, and inform our constitutive model parameters directly from these lower scale simulations (for example, see Refs. [47]–[50]).

Table 1. Model parameters for Fe-Cr-Al alloys.

Parameter	*Value*	*Meaning/Notes*
$\dot{\gamma}_0$, n	$1.0\times10^{4}\,\mathrm{s}^{-1}$, 15	Reference shear rate, inverse of strain rate sensitivity.
G , b	82.5 GPa, $2.48\times10^{-10}\,\mathrm{m}$	Shear modulus (from [51]), Burger vector magnitude.
σ_0 , k_{HP}	316 MPa, 1200 $\mathrm{MPa}\sqrt{\mu\mathrm{m}}$	Lattice friction resistance, Hall-Petch coefficient
$A^{\kappa\kappa}$, $A^{\kappa\zeta}\left(\kappa\neq\zeta\right)$, h_ρ , h_{111}, h_{100} , $h_{\alpha'}$	1.0, 0.2, 0.37, 0.6, 0.6, 0.4	Dislocation self-hardening coefficient, latent hardening coefficient, hardening coefficients related to line dislocations, <111> loops, <100> loops, and α' precipitates, respectively.
k_{mul} , R_c , k_{dyn} , β_ρ , β_{111}, β_{100} , $\beta_{\alpha'}$	0.15, $7.5\times10^{-10}\,\mathrm{m}$, 300.0, 0.3, 0.4, 0.4, 0.2	Dislocation multiplication constant, capture radius for mutual annihilation of dislocation dipoles, dynamic recovery constant, trapping coefficients related to line dislocations, <111> loops, <100> loops, and α' precipitates, respectively.
R^{κ}_{111}, R^{κ}_{100} , $R^{\kappa}_{\alpha'}$, c	$7d^{\kappa}_{111}$, $7d^{\kappa}_{100}$, $7d^{\kappa}_{\alpha'}$, 0.8	Capture radii associated with the annihilation of <111> loops, <100> loops, and α' precipitates by mobile dislocations, and associated annihilation exponent.

Table 2. Initial values of grain size and ISVs on each slip system for various Fe-Cr-Al alloys based on data from Refs. [13], [14]. Note that the black dots (denoted by the subscript BD) are assumed to be equally distributed among <111> and <100> loops.

Alloy	Dose (dpa)	D (μm)	ρ_M^0 (m^{-2})	ρ_I^0 (m^{-2})	N_{111}^0 (m^{-3}), d_{111}^0 (m)	N_{100}^0 (m^{-3}), d_{100}^0 (m)	$N_{\alpha'}^0$ (m^{-3}), $d_{\alpha'}^0$ (m)	N_{BD}^0 (m^{-3}), d_{BD}^0 (m)
Fe-15Cr-4Al (Cold worked)	0	30	1.0×10^{11}	6.7×10^{12}	-	-	-	-
Fe-15Cr-4Al (Fusion zone)	0	80	1.0×10^{11}	6.7×10^{11}	-	-	-	-
Fe-10Cr-4.8Al (Cold worked)	1.6	30	1.0×10^{11}	4.9×10^{12}	7.1×10^{18}, 3.2×10^{-8}	1.9×10^{18}, 5.2×10^{-8}	8.1×10^{21}, 4.4×10^{-9}	5.8×10^{18}, 9.1×10^{-9}
Fe-12Cr-4.4Al (Cold worked)	1.6	30	1.0×10^{11}	8.9×10^{12}	3.7×10^{19}, 1.9×10^{-8}	9.6×10^{18}, 2.9×10^{-8}	8.2×10^{22}, 3.6×10^{-9}	6.7×10^{19}, 8.2×10^{-9}
Fe-15Cr-3.9Al (Cold worked)	1.6	30	1.0×10^{11}	8.7×10^{12}	1.2×10^{19}, 3.0×10^{-8}	3.5×10^{18}, 4.1×10^{-8}	2.0×10^{23}, 3.6×10^{-9}	1.2×10^{19}, 9.8×10^{-9}
Fe-18Cr-2.9Al (Cold worked)	1.6	30	1.0×10^{11}	7.3×10^{12}	3.5×10^{19}, 2.5×10^{-8}	9.6×10^{18}, 3.2×10^{-8}	2.8×10^{23}, 3.7×10^{-9}	4.2×10^{19}, 8.4×10^{-9}

5. Model Results

5.1. Comparison to Experimental Data

Figure 1 shows the comparison of model predictions of true stress-strain curves with experiments [45] for the virgin Fe-15Cr-4Al alloy. The material was tested in as-worked condition as well as at the fusion zone (with dislocation recovery) at room temperature up to a true strain of 0.4 and 0.2, respectively. As for simulations, an initial texture representative of Fe-Cr alloys was used as an input for VPSC. This texture follows from a rolling test simulation done on an initially random collection of 500 orientations (grains) subjected to 20% rolling reduction. This texture is shown in Fig. 2 and is similar to the experimental texture reported for another ferritic Fe-Cr cladding alloy [52]. The material was loaded along the rolling direction, although not much variation was observed in terms of stress-strain response when loading along the transverse or the normal direction.

A fairly good correlation was obtained to experiments. It should of course be noted that the model parameters were calibrated using these two cases. Based on the model calibration, one surprising aspect was that this material exhibits a strong grain size dependence. The Hall-Petch parameter, k_{HP}, used in our simulations is about 2 times that observed for polycrystalline iron [53]. This model parameter can be fine-tuned, perhaps with data from more systematic experiments.

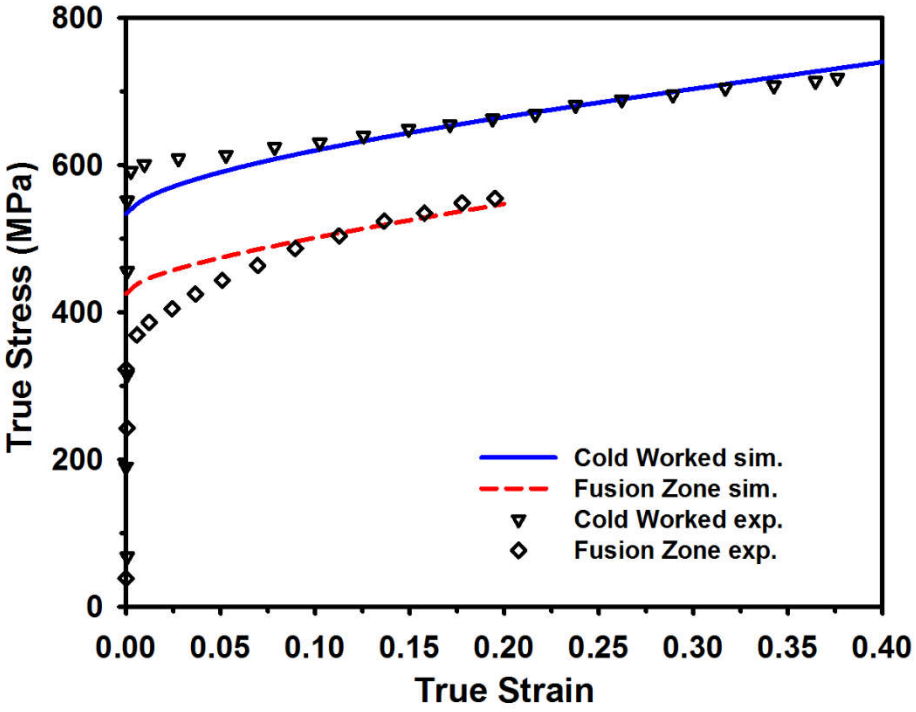

Figure 1. Model predictions of the stress-strain response of cold worked and fusion zone specimens of Fe-15Cr-4Al laser weld alloys compared with experiments [45].

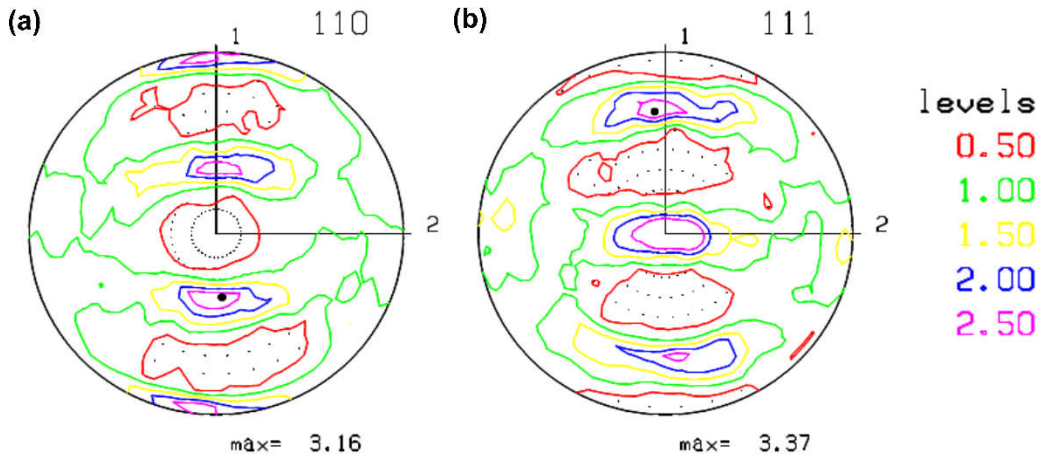

Figure 2. Initial texture used for the cold-worked material obtained after 20% rolling reduction. 1=RD and 2=TD.

Figure 3 shows the comparison of predicted yield stress with experiments for various Fe-Cr-Al alloys irradiated to 1.6 dpa damage [13], [14]. Note that the model was calibrated to experiments only for the irradiated Fe-15Cr-3.9Al alloy. Further, all alloys were assumed to have an initial texture corresponding to that given in Fig. 2. A good correlation is obtained with experiments for all cases, except the irradiated Fe-10Cr-4.8Al alloy. For this case, the model predicts a yield stress that is ≈80 MPa higher than the experimental value. This is an anomalous case, where the experiments reported that the material shows softening post-irradiation. At this moment, the physical reason behind this observation is not completely understood. Nevertheless, the model is able to predict the observed increase in yield stress due to irradiation hardening in all other cases.

Figure 4 shows the true stress-strain response of the irradiated alloys loaded to 0.05 strain. The predicted response is consistent with experiments [13], [14] in that the alloys does not show significant hardening subsequent to initial yield and the stress-strain curves flatten out. A direct comparison with experiments is not possible due to the aforementioned lack of true stress-strain data. In these alloys irradiated to 1.6 dpa, α' precipitates are the dominant irradiation-induced defects. It is possible that interaction of mobile dislocations with the precipitates does not lead to significant dislocation channel clearing and subsequent flow localization; hence the observed flattening of stress-strain response. It is expected that at higher radiation doses, dislocation loops will dominate the irradiated microstructure and will lead to more prolific dislocation channeling, consistent with the deformation behavior observed in other Fe-Cr alloys [30], [54], [55].

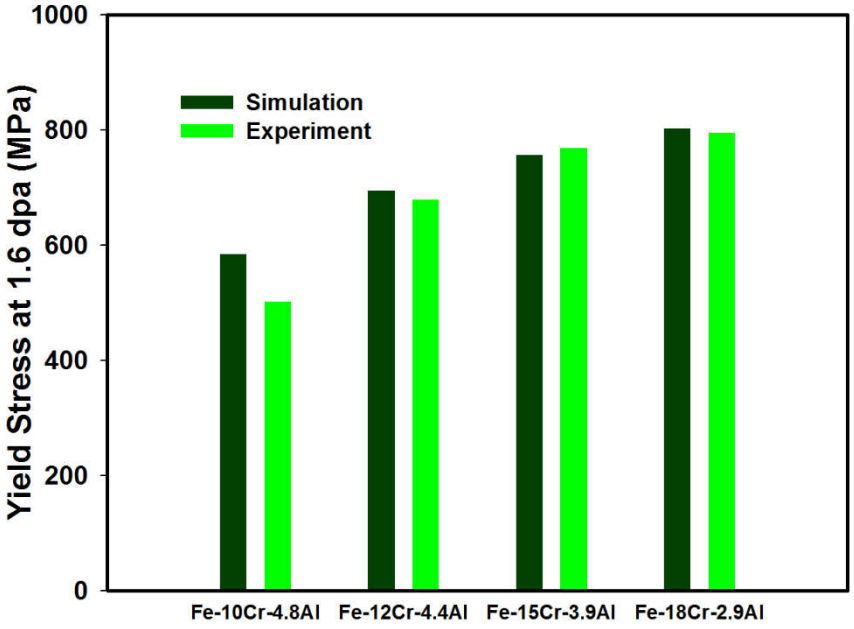

Figure 3. Comparison of the predicted yield stress with experiments [13], [14] for various FeCrAl alloys irradiated to 1.6 dpa damage.

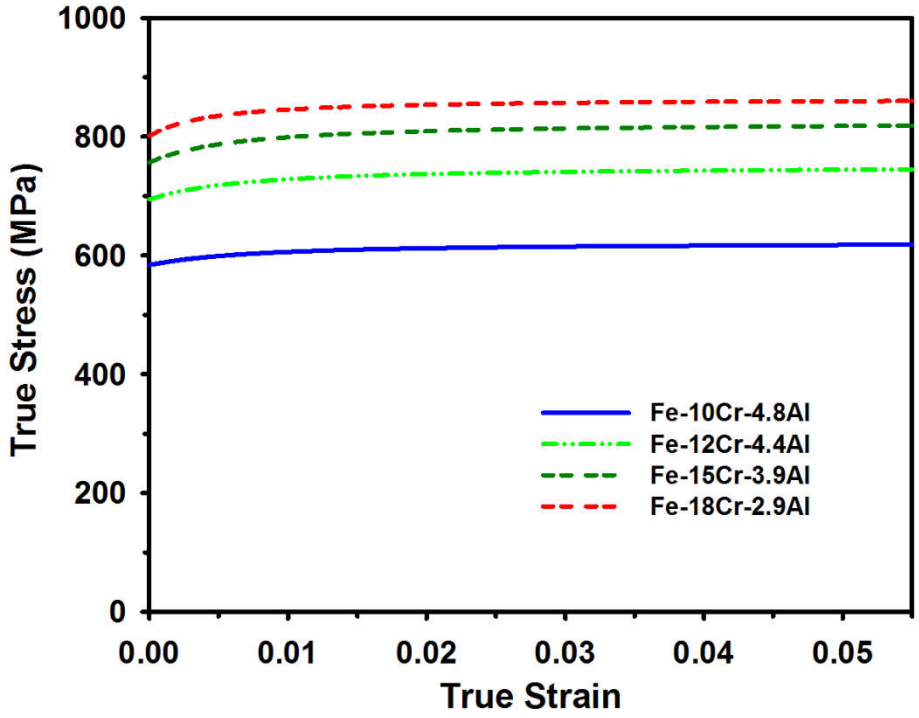

Figure 4. True stress-strain response of FeCrAl alloys irradiated to 1.6 dpa damage.

5.2. Effect of Texture on the Mechanical Response

The model was used to study the effect of texture on the mechanical response. We used various textures as input to the VPSC model: the random texture (shown in Fig. 5), the texture calculated from the rolling simulations with 20% reduction (Fig. 2), and 63% rolling reduction (Fig. 6), respectively. Note that the texture after 63% rolling reduction is extremely sharp as compare to the others. The predicted strain-stress response for virgin and irradiated Fe-15Cr-3.9Al alloy using the three initial textures are given in Fig. 7. It is evident that the sharper initial texture leads to a higher flow stress for both the virgin and irradiated alloys. Moreover, an initial rolling reduction of 20% does not affect the tensile response significantly.

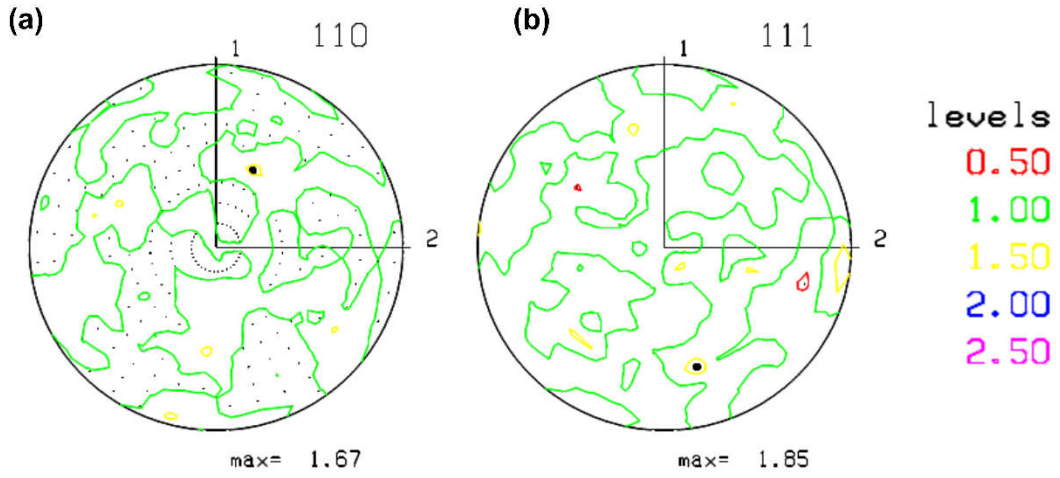

Figure 5. Initial random texture with 500 grains.

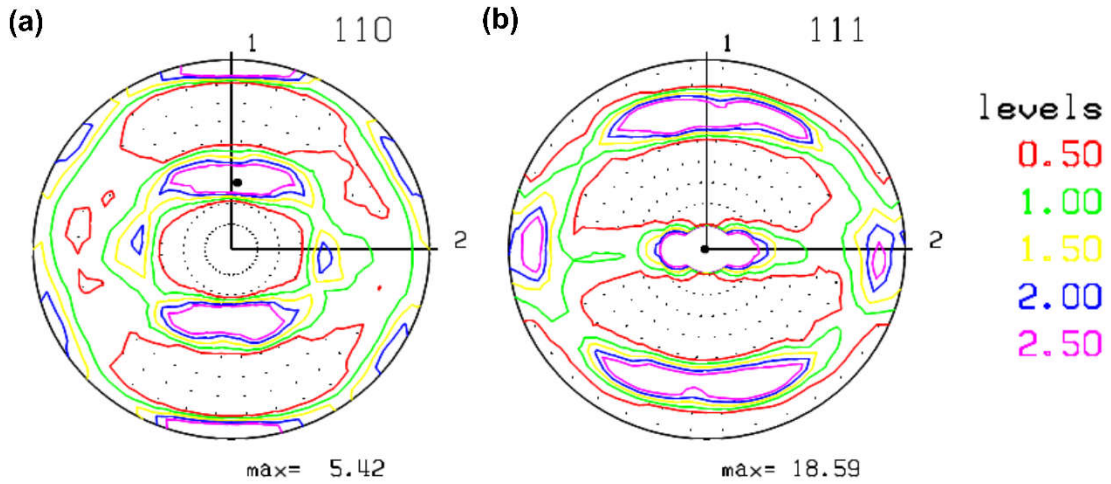

Figure 6. Texture calculated from the rolling tests starting from the random texture with 63% of rolling reduction. Observe that the texture components appear at same position but much sharper than for 22% reduction (Fig. 2). This is used as input to VPSC to study the effect of texture.

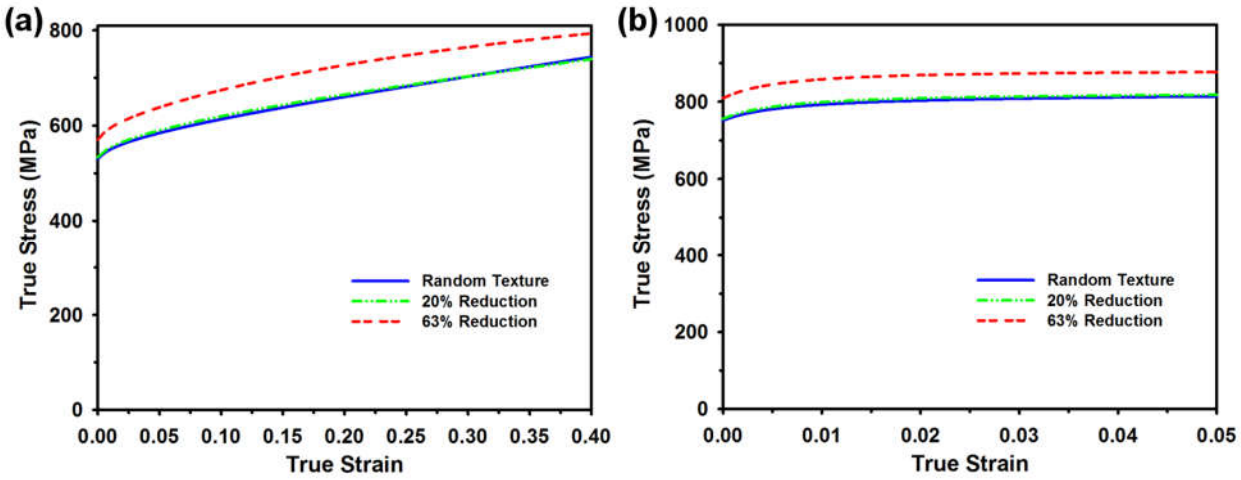

Figure 7. Effect of initial texture on the stress-strain response of (a): virgin, and (b): irradiated (1.6 dpa radiation damage) Fe-15Cr-3.9Al alloy, respectively.

6. Summary and Future Work

We have implemented a defect density-based crystal plasticity model in the VPSC framework to simulate the mechanical response of FeCrAl alloys undergoing irradiation. The model uses line dislocations, irradiation-induced dislocation loops and α' precipitates as state variables, the evolution of which governs the crystallographic deformation mechanisms. Physically-based models are used for the evolution of these state variables. In this initial application, the model parameters were first fit to the available experimental data, and then used to predict stress-strain of FeCrAl alloys with varying composition, and to study the effects of texture on the tensile response.

We are presently working on integrating these models with the MOOSE-BISON finite element code. An interface has been created, and we were expecting to have it up and running with the implementation of the irradiation hardening model described here. However, we are in the process of debugging it because stand-alone VPSC simulations exhibit larger flow stresses than the ones predicted with MOOSE-BISON using the interface. Once in place, this interface will allow us to simulate reactor conditions over a range of deformation, temperature, and radiation histories. Work in the next phase will involve integrating physically-based irradiation and thermal creep models into this framework. Lower scale calculations will be used to understand the physical mechanisms and inform model parameters relating to the dislocation-defect interactions.

References

[1] S. J. Zinkle and Y. Matsukawa, "Observation and analysis of defect cluster production and interactions with dislocations," *Journal of Nuclear Materials*, vol. 329–333, no. Part 1, pp. 88–96, 2004.

[2] A. F. Rowcliffe, J. P. Robertson, R. L. Klueh, K. Shiba, D. J. Alexander, M. L. Grossbeck, and S. Jitsukawa, "Fracture toughness and tensile behavior of ferritic-martensitic steels irradiated at low temperatures," *Journal of Nuclear Materials*, vol. 258–263, no. Part 2, pp. 1275–1279, 1998.

[3] N. Hashimoto, S. J. Zinkle, R. L. Klueh, A. F. Rowcliffe, and K. Shiba, "Deformation Mechanisms in Ferritic/Martensitic Steels Irradiated in HFIR," *Materials Research Society Symposium Proceedings*, vol. 650, p. R1.10, 2001.

[4] M. B. Toloczko and F. A. Garner, "Irradiation creep and void swelling of two LMR heats of HT9 at ~ 400°C and 165 dpa," *Journal of Nuclear Materials*, vol. 233–237, Part 1, pp. 289–292, Oct. 1996.

[5] M. B. Toloczko, F. A. Garner, and C. R. Eiholzer, "Irradiation creep and swelling of the US fusion heats of HT9 and 9Cr-1Mo to 208 dpa at ~ 400°C," *Journal of Nuclear Materials*, vol. 212–215, Part 1, pp. 604–607, Sep. 1994.

[6] C. Lemaignan and A. T. Motta, "Zirconium Alloys in Nuclear Applications," in *Materials Science and Technology*, Wiley-VCH Verlag GmbH & Co. KGaA, 2006.

[7] S. J. Zinkle and N. M. Ghoniem, "Prospects for accelerated development of high performance structural materials," *Journal of Nuclear Materials*, vol. 417, no. 1–3, pp. 2–8, Oct. 2011.

[8] B. A. Pint, K. A. Terrani, M. P. Brady, T. Cheng, and J. R. Keiser, "High temperature oxidation of fuel cladding candidate materials in steam–hydrogen environments," *Journal of Nuclear Materials*, vol. 440, no. 1–3, pp. 420–427, Sep. 2013.

[9] A. Patra and D. L. McDowell, "Continuum modeling of localized deformation in irradiated bcc materials," *Journal of Nuclear Materials*, vol. 432, no. 1–3, pp. 414–427, 2013.

[10] A. Patra and D. L. McDowell, "Crystal plasticity-based constitutive modelling of irradiated bcc structures," *Philosophical Magazine*, vol. 92, no. 7, pp. 861–887, 2012.

[11] R. A. Lebensohn and C. N. Tomé, "A self-consistent anisotropic approach for the simulation of plastic deformation and texture development of polycrystals: application to zirconium alloys," *Acta metallurgica et materialia*, vol. 41, no. 9, pp. 2611–2624, 1993.

[12] C. N. Tomé and R. A. Lebensohn, "Self Consistent Homogenization Methods for Texture and Anisotropy," in *Continuum Scale Simulation of Engineering Materials*, D. Raabe, F. Roters, F. Barlat, and L.-Q. Chen, Eds. Wiley-VCH Verlag GmbH & Co. KGaA, 2004, pp. 473–499.

[13] K. G. Field, X. Hu, K. Littrell, Y. Yamamoto, R. H. Howard, and L. L. Snead, "Stability of Model Fe-Cr-Al Alloys Under The Presence of Neutron Radiation," Oak Ridge National Laboratory (ORNL); High Flux Isotope Reactor (HFIR), 2014.

[14] K. G. Field, X. Hu, K. C. Littrell, Y. Yamamoto, and L. L. Snead, "Radiation tolerance of neutron-irradiated model Fe–Cr–Al alloys," *Journal of Nuclear Materials*, vol. 465, pp. 746–755, Oct. 2015.

[15] U. F. Kocks, A. S. Argon, and M. F. Ashby, *Thermodynamics and kinetics of slip*, vol. 19. Permagon Press, 1975.

[16] V. Vitek, "Structure of dislocation cores in metallic materials and its impact on their plastic behaviour," *Progress in Materials Science*, vol. 36, pp. 1–27, 1992.

[17] V. Vitek and V. Paidar, "Chapter 87 Non-planar dislocation cores: a ubiquitous phenomenon affecting mechanical properties of crystalline materials," in *Dislocations in Solids: A Tribute to F.R.N. Nabarro*, vol. Volume 14, J. P. Hirth, Ed. Elsevier, 2008, pp. 439–514.

[18] A. Patra, T. Zhu, and D. L. McDowell, "Constitutive equations for modeling non-Schmid effects in single crystal bcc-Fe at low and ambient temperatures," *International Journal of Plasticity*, vol. 59, pp. 1–14, 2014.

[19] E. O. Hall, "The Deformation and Ageing of Mild Steel: III Discussion of Results," *Proceedings of the Physical Society. Section B*, vol. 64, no. 9, pp. 747–753, Sep. 1951.

[20] N. J. Petch, "The cleavage strength of polycrystals," *J. Iron Steel Inst.*, vol. 174, pp. 25–28, 1953.

[21] G. R. Odette and D. Frey, "Development of mechanical property correlation methodology for fusion environments," *Journal of Nuclear Materials*, vol. 85–86, no. Part 2, pp. 817–822, 1979.
[22] G. E. Lucas, "The evolution of mechanical property change in irradiated austenitic stainless steels," *Journal of Nuclear Materials*, vol. 206, no. 2–3, pp. 287–305, 1993.
[23] U. Essmann and H. Mughrabi, "Annihilation of dislocations during tensile and cyclic deformation and limits of dislocation densities," *Philosophical Magazine A*, vol. 40, no. 6, pp. 731–756, 1979.
[24] F. Roters, D. Raabe, and G. Gottstein, "Work hardening in heterogeneous alloys--a microstructural approach based on three internal state variables," *Acta Materialia*, vol. 48, no. 17, pp. 4181–4189, 2000.
[25] Y. Estrin and L. P. Kubin, "Local strain hardening and nonuniformity of plastic deformation," *Acta Metallurgica*, vol. 34, no. 12, pp. 2455–2464, 1986.
[26] R. A. Austin and D. L. McDowell, "A dislocation-based constitutive model for viscoplastic deformation of fcc metals at very high strain rates," *International Journal of Plasticity*, vol. 27, no. 1, pp. 1–24, 2011.
[27] J. Kacher, G. S. Liu, and I. M. Robertson, "In situ and tomographic observations of defect free channel formation in ion irradiated stainless steels," *Micron*, vol. 43, no. 11, pp. 1099–1107, Nov. 2012.
[28] J. S. Robach, I. M. Robertson, B. D. Wirth, and A. Arsenlis, "In-situ transmission electron microscopy observations and molecular dynamics simulations of dislocation-defect interactions in ion-irradiated copper," *Philosophical Magazine*, vol. 83, no. 8, pp. 955–967, 2003.
[29] I. M. Robertson, A. Beaudoin, K. Al-Fadhalah, L. Chun-Ming, J. Robach, B. D. Wirth, A. Arsenlis, D. Ahn, and P. Sofronis, "Dislocation-obstacle interactions: Dynamic experiments to continuum modeling," *Materials Science and Engineering A*, vol. 400–401, pp. 245–250, 2005.
[30] D. S. Gelles and R. E. Schäublin, "Post-irradiation deformation in a Fe-9%Cr alloy," *Materials Science and Engineering: A*, vol. 309–310, pp. 82–86, 2001.
[31] T. Nogaret, D. Rodney, M. Fivel, and C. Robertson, "Clear Band formation simulated by dislocation dynamics," *Problems of Atomic Science and Technology*, vol. 4, pp. 97–108, 2009.
[32] T. Nogaret, D. Rodney, M. Fivel, and C. Robertson, "Clear band formation simulated by dislocation dynamics: Role of helical turns and pile-ups," *Journal of Nuclear Materials*, vol. 380, no. 1–3, pp. 22–29, 2008.
[33] D. Terentyev, D. J. Bacon, and Y. N. Osetsky, "Reactions between a 1/2⟨111⟩ screw dislocation and ⟨100⟩ interstitial dislocation loops in alpha-iron modelled at atomic scale," *Philosophical Magazine*, vol. 90, no. 7–8, pp. 1019–1033, 2010.
[34] D. J. Bacon, Y. N. Osetsky, and Z. Rong, "Computer simulation of reactions between an edge dislocation and glissile self-interstitial clusters in iron," *Philosophical Magazine*, vol. 86, no. 25–26, pp. 3921–3936, 2006.
[35] B. D. Wirth, V. V. Bulatov, and T. D. de la Rubia, "Dislocation-Stacking Fault Tetrahedron Interactions in Cu," *Journal of Engineering Materials and Technology*, vol. 124, no. 3, pp. 329–334, 2002.
[36] A. Luft, "Microstructural processes of plastic instabilities in strengthened metals," *Progress in Materials Science*, vol. 35, no. 2, pp. 97–204, 1991.
[37] A. J. E. Foreman and J. V. Sharp, "A mechanism for the sweeping-up of loops by glide dislocations during deformation," *Philosophical Magazine*, vol. 19, no. 161, pp. 931–937, 1969.
[38] S. J. Zinkle and B. N. Singh, "Microstructure of neutron-irradiated iron before and after tensile deformation," *Journal of Nuclear Materials*, vol. 351, no. 1–3, pp. 269–284, 2006.
[39] J. V. Sharp, "Deformation of neutron irradiated copper alloys," *Acta Metallurgica*, vol. 22, no. 4, pp. 449–457, Apr. 1974.
[40] T. S. Byun, N. Hashimoto, K. Farrell, and E. H. Lee, "Characteristics of microscopic strain localization in irradiated 316 stainless steels and pure vanadium," *Journal of Nuclear Materials*, vol. 349, no. 3, pp. 251–264, Mar. 2006.

[41] K. Farrell, T. S. Byun, and N. Hashimoto, "Deformation mode maps for tensile deformation of neutron-irradiated structural alloys," *Journal of Nuclear Materials*, vol. 335, no. 3, pp. 471–486, Dec. 2004.
[42] A. Arsenlis, M. Rhee, G. Hommes, R. Cook, and J. Marian, "A dislocation dynamics study of the transition from homogeneous to heterogeneous deformation in irradiated body-centered cubic iron," *Acta Materialia*, vol. 60, no. 9, pp. 3748–3757, May 2012.
[43] R. A. Lebensohn, C. N. Tomé, and P. P. CastaÑeda, "Self-consistent modelling of the mechanical behaviour of viscoplastic polycrystals incorporating intragranular field fluctuations," *Philosophical Magazine*, vol. 87, no. 28, pp. 4287–4322, Oct. 2007.
[44] H. Wang, B. Raeisinia, P. D. Wu, S. R. Agnew, and C. N. Tomé, "Evaluation of self-consistent polycrystal plasticity models for magnesium alloy AZ31B sheet," *International Journal of Solids and Structures*, vol. 47, no. 21, pp. 2905–2917, Oct. 2010.
[45] K. G. Field, M. N. Gussev, Y. Yamamoto, and L. L. Snead, "Deformation behavior of laser welds in high temperature oxidation resistant Fe–Cr–Al alloys for fuel cladding applications," *Journal of Nuclear Materials*, vol. 454, no. 1–3, pp. 352–358, Nov. 2014.
[46] K. Kitayama, C. N. Tomé, E. F. Rauch, J. J. Gracio, and F. Barlat, "A crystallographic dislocation model for describing hardening of polycrystals during strain path changes. Application to low carbon steels," *International Journal of Plasticity*, vol. 46, pp. 54–69, Jul. 2013.
[47] E. Martinez, J. Marian, and J. M. Perlado, "A dislocation dynamics study of the strength of stacking fault tetrahedra. Part II: interactions with mixed and edge dislocations," *Philosophical Magazine*, vol. 88, no. 6, pp. 841–863, 2008.
[48] E. Martinez, J. Marian, A. Arsenlis, M. Victoria, and J. M. Perlado, "A dislocation dynamics study of the strength of stacking fault tetrahedra. Part I: interactions with screw dislocations," *Philosophical Magazine*, vol. 88, no. 6, pp. 809–840, 2008.
[49] D. Li, H. Zbib, H. Garmestani, X. Sun, and M. Khaleel, "Modeling of irradiation hardening of polycrystalline materials," *Computational Materials Science*, vol. 50, no. 8, pp. 2496–2501, 2011.
[50] N. R. Barton, A. Arsenlis, and J. Marian, "A polycrystal plasticity model of strain localization in irradiated iron," *Journal of the Mechanics and Physics of Solids*, vol. 61, no. 2, pp. 341–351, 2013.
[51] S. Naamane, G. Monnet, and B. Devincre, "Low temperature deformation in iron studied with dislocation dynamics simulations," *International Journal of Plasticity*, vol. 26, no. 1, pp. 84–92, 2010.
[52] C. Deo, C. Tomé, R. Lebensohn, and S. Maloy, "Modeling and simulation of irradiation hardening in structural ferritic steels for advanced nuclear reactors," *Journal of Nuclear Materials*, vol. 377, no. 1, pp. 136–140, 2008.
[53] S. Takaki, D. Akama, N. Nakada, and T. Tsuchiyama, "Effect of Grain Boundary Segregation of Interstitial Elements on Hall–Petch Coefficient in Steels," *Materials Transactions*, vol. 55, no. 1, pp. 28–34, 2014.
[54] R. Chaouadi, "Effect of irradiation-induced plastic flow localization on ductile crack resistance behavior of a 9%Cr tempered martensitic steel," *Journal of Nuclear Materials*, vol. 372, no. 2–3, pp. 379–390, 2008.
[55] M. I. Luppo, C. Bailat, R. Schäublin, and M. Victoria, "Tensile properties and microstructure of 590 MeV proton-irradiated pure Fe and a Fe-Cr alloy," *Journal of Nuclear Materials*, vol. 283–287, no. Part 1, pp. 483–487, 2000.